INTERNATIONAL JOURNAL FOR NUMERICAL METHODS IN FLUIDS
Int. J. Numer. Meth. Fluids 2010; **62**:784–801
Published online 8 April 2009 in Wiley InterScience (www.interscience.wiley.com). DOI: 10.1002/fld.2044

An implicit method for the Navier–Stokes equations on overlapping block-structured grids

E. Ahusborde*, † and S. Glockner

Laboratoire TREFLE, Université de Bordeaux, CNRS-UMR 8508, 16 av. Pey-Berland, 33607 Pessac Cedex, France

SUMMARY

This paper deals with a method first introduced by Romé *et al.* in two articles. The authors reported that their method was suitable to run the Navier–Stokes equations efficiently on non-matching and overlapping block-structured meshes. However, there was a problem of mass conservation and a discontinuity of pressure through the interfaces in some cases. In the present paper, an improvement of the method based on a pressure correction scheme is proposed. With this improvement, the pressure is continuous through the interfaces and the incompressibility constraint is ensured over the whole domain. Several numerical tests were carried out to assess the proposed method. Copyright © 2009 John Wiley & Sons, Ltd.

Received 5 November 2008; Revised 13 February 2009; Accepted 13 February 2009

KEY WORDS: block-structured meshes; Navier–Stokes; non-conforming; non-matching; overlapping; interpolation

1. INTRODUCTION

In computational fluid dynamics when flows are calculated for complex geometries, one can either use a block-structured grid or an unstructured one. Unstructured grids allow very complex geometries to be meshed leading to complex discretization schemes and solvers that require tables of connectivity between nodes and indirect addressing. If the geometry is not too complicated, it can be divided into a reasonable number of structured blocks. Lexical numbering facilitates the discretization of the equations (specially if the grid remains orthogonal) and the use of many solvers dedicated to the structured grids.

*Correspondence to: E. Ahusborde, Laboratoire TREFLE, Université de Bordeaux, CNRS-UMR 8508, 16 av. Pey-Berland, 33607 Pessac Cedex, France.
†E-mail: ahusborde@enscpb.fr

Contract/grant sponsor: Conseil Régional d'Aquitaine
Contract/grant sponsor: French Ministry of Science and Technology

Domain decomposition methods are well suited to these issues. They can be classified according to several criteria [1]. For instance, the block-structured grids can be overlapping or non-overlapping. Generally, each block is computed separately and provides the boundary conditions for the neighbouring blocks. Historically, these methods have been introduced by Schwarz [2]. The main drawback of the method is that overlapping is required for convergence. An improvement consists in substituting overlapping by another boundary condition. In [3], Lions proposed the use of a Robin boundary condition. Our strategy consists in working with overlapping in order to deal with orthogonal grids. The main difficulty is to find a relevant projection operator on the interfaces between sub-domains. Mortar element methods have been proposed to solve this problem [4, 5]. Chimera methods represent another approach [6, 7]. These methods are particularly used in aerodynamic simulations.

Non-matching meshes raise the classical question of interpolation. This difficulty becomes harder when the interpolation has to be carried out under constraint. In the case of simulation of an incompressible flow, the constraint $\nabla\cdot\mathbf{u}=0$ must be verified. Generally, interpolation is conservative if it is based on finite volume techniques [8, 9]. Fluxes through interfaces are calculated using local balance with a neighbouring block or a projection. Recently, a mass-flux-based interpolation algorithm was proposed by Tang *et al.* [10, 11]. Some authors who used non-conservative interpolation have shown that mass conservation is directly linked to the order of the interpolation [12].

In this paper, we propose an implicit method to compute the incompressible Navier–Stokes equations on block-structured meshes based on non-conservative interpolation. This study proposes an improvement of the method first introduced in [13, 14]. Indeed, the authors previously met problems to satisfy the incompressibility constraint on the interfaces between blocks leading in some cases to a discontinuity of pressure. They used the augmented Lagrangian method [15] for pressure–velocity coupling. In the present case, the method has been replaced by a pressure correction scheme [16] to circumvent these drawbacks.

We first present the numerical context of the study by describing the models and numerical methods of the CFD code Aquilon (Aq. in figures and tables). Then, we describe the novelties of the method in comparison with the method first introduced in [13, 14]. Finally, numerical tests were carried out to validate the method and clearly show the improvements.

2. NUMERICAL CONTEXT

2.1. Numerical methods

In this paper, the incompressible Navier–Stokes equations are considered:

Find the velocity $\mathbf{u}$ *and the pressure* p *such that*:

$$\nabla\cdot\mathbf{u}=0 \quad \text{in } \Omega \tag{1}$$

$$\rho\left(\frac{\partial\mathbf{u}}{\partial t}+\nabla\cdot(\mathbf{u}\otimes\mathbf{u})\right)=-\nabla p+\nabla\cdot\mu(\nabla\mathbf{u}+\nabla^t\mathbf{u}) \quad \text{in } \Omega \tag{2}$$

$$\mathbf{u}=\mathbf{0} \quad \text{on } \partial\Omega \tag{3}$$

where ρ is the density of the fluid, μ is the dynamic viscosity and $\Omega\subset\mathbb{R}^2$ is a bounded open domain with Lipschitzian border $\partial\Omega$.

DOI: 10.1002/fld

The main difficulty in the resolution of the problem (1)–(3) consists in ensuring the incompressibility constraint that couples the velocity and the pressure. In the previous study [14], the augmented Lagrangian method [15] was dealt with. In the present study, we will focus on a pressure correction scheme [16].

2.1.1. The pressure correction scheme. The pressure correction time integration scheme consists in splitting the Navier–Stokes system into two stages, a velocity prediction and a pressure correction [16]. The time interval $[0, T]$ is divided into N equidistant time steps of length $\Delta t = T/N$. The approximate velocity and pressure fields at time $t^n = n\Delta t$ $(n = 0, \ldots, N)$ are denoted $\mathbf{u}^n$ and p^n, respectively. Assuming all quantities are known up to t^n, the solution at t^{n+1} results from the velocity prediction step:

Find $\mathbf{u}_*^{n+1}$ *such that*:

$$\rho\left(\frac{\mathbf{u}_*^{n+1}-\mathbf{u}^n}{\Delta t}+\nabla\cdot(\mathbf{u}_*^{n+1}\otimes\mathbf{u}^n)-\mathbf{u}_*^{n+1}\nabla\cdot\mathbf{u}^n\right)=-\nabla p^n+\nabla\cdot\mu(\nabla\mathbf{u}_*^{n+1}+\nabla^t\mathbf{u}_*^{n+1}) \quad \text{in } \Omega \tag{4}$$

$$\mathbf{u}_*^{n+1}=\mathbf{0} \quad \text{on } \partial\Omega \tag{5}$$

followed by the pressure correction step:

Find $\mathbf{u}^{n+1}$ *and* ϕ^{n+1} *such that*:

$$\rho\frac{\mathbf{u}^{n+1}-\mathbf{u}_*^{n+1}}{\Delta t}+\nabla\phi^{n+1}=\mathbf{0} \quad \text{in } \Omega \tag{6}$$

$$\nabla\cdot\mathbf{u}^{n+1}=0 \quad \text{in } \Omega \tag{7}$$

$$\mathbf{u}^{n+1}\cdot\mathbf{n}=0 \quad \text{on } \partial\Omega \tag{8}$$

with:

$$\phi^{n+1}=p^{n+1}-p^n+\mu\nabla\cdot\mathbf{u}_*^{n+1} \tag{9}$$

Considering ρ constant and taking the divergence of (6) gives:

$$\Delta\phi^{n+1}=\frac{\rho}{\Delta t}\nabla\cdot\mathbf{u}_*^{n+1} \quad \text{in } \Omega \tag{10}$$

$$\left.\frac{\partial\phi}{\partial\mathbf{n}}\right|^{n+1}=0 \quad \text{on } \partial\Omega \tag{11}$$

Once ϕ^{n+1} is computed, the divergence-free velocity and the pressure are obtained by:

$$\mathbf{u}^{n+1}=\mathbf{u}_*^{n+1}-\frac{\Delta t}{\rho}\nabla\phi^{n+1} \tag{12}$$

$$p^{n+1}=\phi^{n+1}+p^n-\mu\nabla\cdot\mathbf{u}_*^{n+1} \tag{13}$$

2.1.2. Spatial discretization. The spatial discretization is based on the finite volume method on a velocity–pressure staggered grid of the Marker and Cells type [17]. Pressure unknowns are associated with the cell vertices, whereas velocity components are face centred. A centred scheme of order 2 is used in this study for the inertial and constraint terms.

DOI: 10.1002/fld

The multifrontal sparse direct solver MUMPS [18] is used to solve the linear systems stemming from the velocity prediction and pressure correction steps. BiCGStab(2) coupled with ILUT preconditioner was also successfully tested.

3. AN IMPLICIT METHOD FOR CONNECTING BLOCKS

In order to connect the sub-domain, the missing information is transferred from block to block. Polynomial interpolations are built and integrated as special boundary conditions. The polynomial coefficients of the interpolation are present in the linear system and couple the solution on each block through the interface. The non-conservative interpolation of the variables at the interfaces can be seen as a new implicit boundary condition used for the discretization of the equation at the nodes strictly inside the different blocks.

3.1. Pressure correction step

Two blocks (a) and (b) are considered (see Figure 1). The pressure increment ϕ defined on block (b) is interpolated, which gives the new boundary conditions on block (a). Interpolation is based on the construction of a polynomial basis of a given order. For instance, the interpolation of ϕ at point $M_0(x_0, y_0)$ belonging to block (a) is obtained from the values of ϕ at points $M_i(x_i, y_i)$ on block (b) by the relation:

$$\phi^{(a)}(x_0, y_0) = f_{\text{int}}(\phi^{(b)}) = \sum_{i=1}^{N} F_i(x_0, y_0)\phi^{(b)}(x_i, y_i) \tag{14}$$

The interpolation must now be constructed locally to each node at the interface. The technique consists in building a canonical basis of Q-type of order d, thanks to the neighbourhood of $M_0(x_0, y_0)$. The number of nodes required depends on the order of the chosen polynomial. For instance, for a $Q^{(1)}$ interpolation Figure 1 represents the interpolation of the pressure on node M_0 belonging to the interface of block (a) obtained from the values of pressure on nodes M_1, M_2, M_3 and M_4 belonging to block (b).

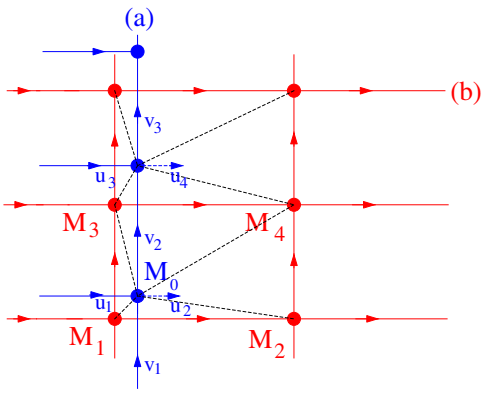

Figure 1. Interpolation of the pressure.

DOI: 10.1002/fld

In order to reduce the values of the coefficients of the polynomial, M_0 is chosen as the centre of the frame. A polynomial $Q_i^{(d)}$ built using the M_i nodes, $1 \leqslant i \leqslant (d+1)^2$ is written:

$$Q_i^{(d)}(x-x_0, y-y_0) = \sum_{m=0}^{d} \sum_{n=0}^{d} a_{mni}(x-x_0)^m (y-y_0)^n \tag{15}$$

$Q_i^{(d)}$ has the following properties:

$$\forall i, j \quad 1 \leqslant i, \quad j \leqslant (d+1)^2, \quad Q_i^{(d)}(x_j - x_0, y_j - y_0) = \delta_{ij} \tag{16}$$

Equation (15) associated with the property (16) can be seen as a line of the $(d+1)^2 \times (d+1)^2$ linear system $A \times B = Id$ with:

$$A = \begin{bmatrix} a_{001} & \cdots & a_{mn1} & \cdots & a_{dd1} \\ \vdots & & \vdots & & \vdots \\ a_{00i} & \cdots & a_{mni} & \cdots & a_{ddi} \\ \vdots & & \vdots & & \vdots \\ a_{00(d+1)^2} & \cdots & a_{mn(d+1)^2} & \cdots & a_{dd(d+1)^2} \end{bmatrix}$$

and

$$B = \begin{bmatrix} (x_1-x_0)^0(y_1-y_0)^0 & \cdots & (x_i-x_0)^0(y_i-y_0)^0 & \cdots & (x_{(d+1)^2}-x_0)^0(y_{(d+1)^2}-y_0)^0 \\ \vdots & & \vdots & & \vdots \\ (x_1-x_0)^m(y_1-y_0)^n & \cdots & (x_i-x_0)^m(y_i-y_0)^n & \cdots & (x_{(d+1)^2}-x_0)^m(y_{(d+1)^2}-y_0)^n \\ \vdots & & \vdots & & \vdots \\ (x_1-x_0)^d(y_1-y_0)^d & \cdots & (x_i-x_0)^d(y_i-y_0)^d & \cdots & (x_{(d+1)^2}-x_0)^d(y_{(d+1)^2}-y_0)^d \end{bmatrix}$$

The inversion of this linear system (one for each node of the interface) is performed during the preparation step of a simulation and provides the values of the matrix A. The value of the pressure ϕ at node $M_0(x_0, y_0)$ reads:

$$\phi^{(a)}(x_0, y_0) = \sum_{i=1}^{(d+1)^2} Q_i^{(d)}(x_0, y_0)\phi^{(b)}(x_i, y_i) \tag{17}$$

The $Q_i^{(d)}$ can be placed in the linear system of the pressure correction step (see Figure 2).

Thus, on a matrix line corresponding to a node at the interface, non-zero elements are the diagonal term and the elements with a column number corresponding to unknowns used to interpolate the pressure.

With this method, the pressure is obviously continuous at the interfaces (up to the order of the polynomial interpolation), but the divergence of the velocity is not null at the interfaces since the velocities u_2, u_4, v_1, v_2 and v_3 (see Figure 1) are not corrected by the pressure correction. Indeed,

DOI: 10.1002/fld

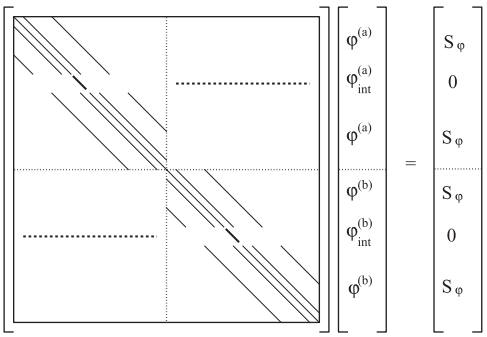

Figure 2. Representation of the pressure correction matrix on 2 blocks.

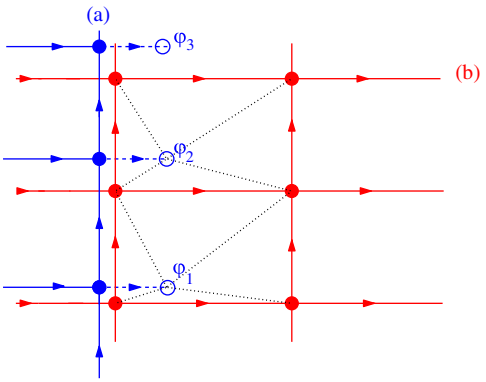

Figure 3. New stencil to ensure incompressibility constraint.

the pressure gradient cannot be well computed on these nodes and introduces an error in Equation (12). In order to circumvent this problem, we propose to increase the overlap between blocks by adding a row of ghost nodes (nodes ϕ_1, ϕ_2 and ϕ_3 in Figure 3). The pressure is now connected from one block to another, thanks to these ghost nodes. The pressure gradient can be computed precisely on velocity nodes at the interfaces. This addition satisfies incompressibility constraint. Nonetheless, the pressure is no longer continuous at the interface. This is probably due to the error in the interpolation of ϕ^{n+1} on the ghost nodes that accumulates on the pressure nodes p^{n+1} at the interface. In order to overcome this problem, a new pressure correction scheme is proposed. The velocity prediction step does not change, but the pressure correction step is modified and a third interpolation step is added. The new scheme reads as follows:

- Velocity prediction step: *Find* $\mathbf{u}_*^{n+1}$ *such that*

$$\rho\left(\frac{\mathbf{u}_*^{n+1}-\mathbf{u}^n}{\Delta t}+\nabla\cdot(\mathbf{u}_*^{n+1}\otimes\mathbf{u}^n)-\mathbf{u}_*^{n+1}\nabla\cdot\mathbf{u}^n\right)=-\nabla p^n+\nabla\cdot\mu(\nabla\mathbf{u}_*^{n+1}+\nabla^t\mathbf{u}_*^{n+1}) \quad \text{in } \Omega \tag{18}$$

$$\mathbf{u}_*^{n+1}=\mathbf{0} \quad \text{on } \partial\Omega \tag{19}$$

DOI: 10.1002/fld

- Pressure correction step: *Find* $\mathbf{u}^{n+1}$ and ϕ^{n+1} such that

$$\rho\frac{\mathbf{u}^{n+1}-\mathbf{u}_*^{n+1}}{\Delta t}+\nabla\phi^{n+1}=\mathbf{0} \quad \text{in } \Omega \tag{20}$$

$$\nabla\cdot\mathbf{u}^{n+1}=0 \quad \text{in } \Omega \tag{21}$$

$$\mathbf{u}^{n+1}\cdot\mathbf{n}=0 \quad \text{on } \partial\Omega \tag{22}$$

  with:

$$\phi^{n+1}=\tilde{p}^{n+1}-p^n+\mu\nabla\cdot\mathbf{u}_*^{n+1} \tag{23}$$

- Interpolation step: *Compute* p^{n+1} *such that*

$$p^{n+1}=\tilde{p}^{n+1} \quad \text{in } \Omega/\Gamma \tag{24}$$

$$p^{n+1}=f_{\text{int}}(\tilde{p}^{n+1}) \quad \text{on } \Gamma \tag{25}$$

  where Γ is the whole interface between blocks and f_{int} represents the interpolation function on Γ.

This new scheme ensures continuity of the pressure through the interfaces and still respects the incompressibility constraint.

3.2. *Velocity prediction step*

Interpolation of the velocity is more difficult since it is a vector field. If the blocks do not have the same orientation, both velocity components are needed to compute a single component of the velocity field on the interface. For a precise description of the method, particularly the interpolation technique on cartesian blocks with any orientation or on curvilinear blocks, the reader is referred to [14]. Previously, the interpolation of the normal component of the velocity field at the interface was performed on pressure nodes, whereas the tangential component was interpolated at the velocity nodes. In the present case, both components are interpolated at the velocity nodes (see Figure 4 in case of a $Q^{(1)}$ interpolation).

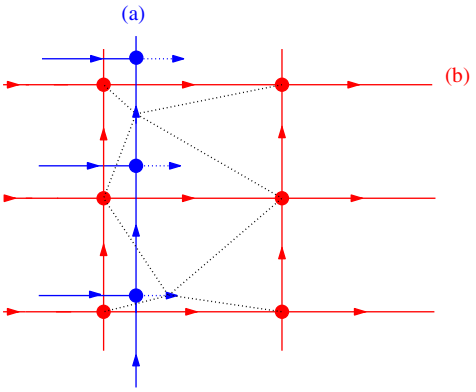

Figure 4. New interpolation of the velocity vector on a staggered grid.

DOI: 10.1002/fld

In the next section, many computations have been carried out to assess the proposed method and to exhibit its improvements in comparison with [14]. $Q^{(2)}$ polynomial interpolation has been systematically used. This leads to a 5-point stencil for pressure and to a 24-point stencil for velocity.

4. NUMERICAL RESULTS

In this section, a series of numerical experiments was performed to evaluate the accuracy and the efficiency of the method. The test cases considered include steady and unsteady flows. First, we consider a Poiseuille flow and the Green–Taylor vortex example to verify the spatial and time order of convergence of the method. Then, the lid-driven cavity is studied to assess the improvement of the method in comparison with [14]. Finally, flows past a two-dimensional obstacle and past a triangular cylinder are considered.

4.1. Poiseuille flow

Simulations were carried out in several non-conforming block-structured meshes represented in Figure 5. The Reynolds number is $Re = 100$. At the inlet, we impose a parabolic profile for the axial velocity u and zero for the velocity v, whereas at the outlet, a Neumann condition is imposed on both velocity components. Since the analytical solution is order 2, the errors are close to computer accuracy if a $Q^{(2)}$ interpolation is used.

4.2. Green–Taylor vortex

The main point of interest with this flow is that, unlike in Poiseuille flow, the inertial term is not null. The Green–Taylor vortex is modified to obtain a stationary solution not identically null [19]. In [14], the authors could not validate the pressure because the divergence of the velocity was not null and accumulated in the pressure. We will see that the new scheme proposed clearly improves these inconveniences.

The momentum equations are enriched by the following source term:

$$\mathbf{S} = \begin{cases} -\dfrac{\pi^2 \mu}{2H^2} \cos\left(\dfrac{\pi x}{2H}\right) \sin\left(\dfrac{\pi y}{2H}\right) \\ -\dfrac{\pi^2 \mu}{2H^2} \sin\left(\dfrac{\pi x}{2H}\right) \cos\left(\dfrac{\pi y}{2H}\right) \end{cases}$$

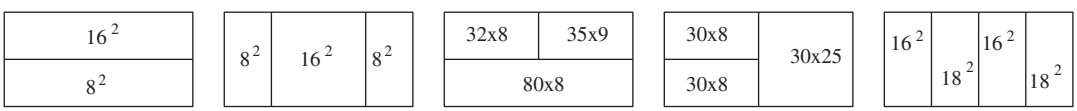

Figure 5. Representation of the different blocks for Poiseuille flow study (number of elements is indicated).

DOI: 10.1002/fld

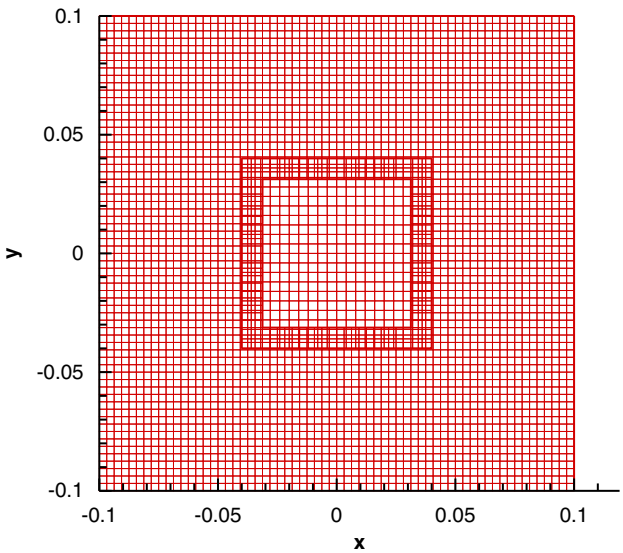

Figure 6. Block-structured mesh for the Green–Taylor flow study.

The solution is:

$$u(x,y,t) = -\cos\left(\frac{\pi x}{2H}\right)\sin\left(\frac{\pi y}{2H}\right)(1-\mathrm{e}^{-\pi^2 \nu t/2H^2})$$

$$v(x,y,t) = +\sin\left(\frac{\pi x}{2H}\right)\cos\left(\frac{\pi y}{2H}\right)(1-\mathrm{e}^{-\pi^2 \nu t/2H^2})$$

$$p(x,y,t) = -\frac{\rho}{2}\left(\cos^2\left(\frac{\pi x}{2H}\right)+\cos^2\left(\frac{\pi y}{2H}\right)\right)(1-2\mathrm{e}^{-\pi^2 \nu t/2H^2}+\mathrm{e}^{-\pi^2 \nu t/H^2})$$

The boundary conditions are obtained directly from the analytical solution and are modified at each time step. The test case was run with two non-conforming structured blocks (see Figure 6).

A time convergence study was carried out. Figure 7 represents the errors at time $T=1\,\mathrm{s}$ as a function of the time step Δt. We observe a slope in log/log scale equal to 1 that is coherent with the order of the scheme used (Euler time scheme and linearization at order 1).

4.3. Lid-driven cavity

The lid-driven cavity problem has long been used as a test or validation case for new codes or new methods. The standard case is fluid contained in a square domain with three wall sides and one moving side (with velocity tangential to the side). In the present paper, we refer to the works of Botella and Peyret [20]. For this computation, a Reynolds number of 1000 is used.

The mesh is divided into five non-conforming structured blocks: the first block occupies the main part of the domain; the lower (upper) blocks have step spaces a third (half) the size of the main block (see Figure 8). The mesh is refined in the corners to have a better description of the flow. The refinement is clearly a strong point of the multiblock strategy. The number of elements is 121 344.

DOI: 10.1002/fld

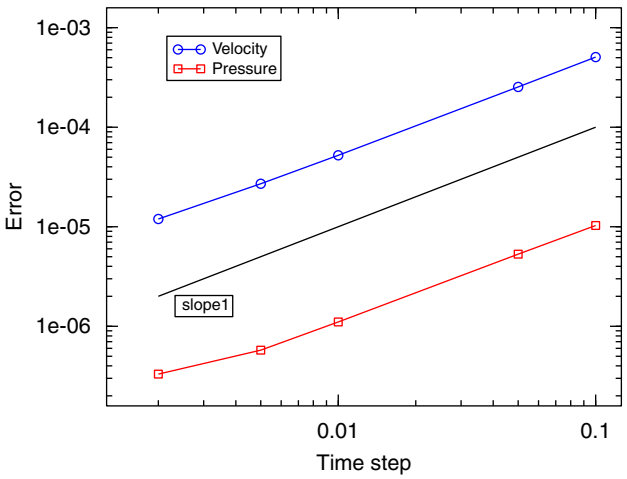

Figure 7. $L^2(\Omega)$ error norm as a function of the time step for the Green–Taylor flow study.

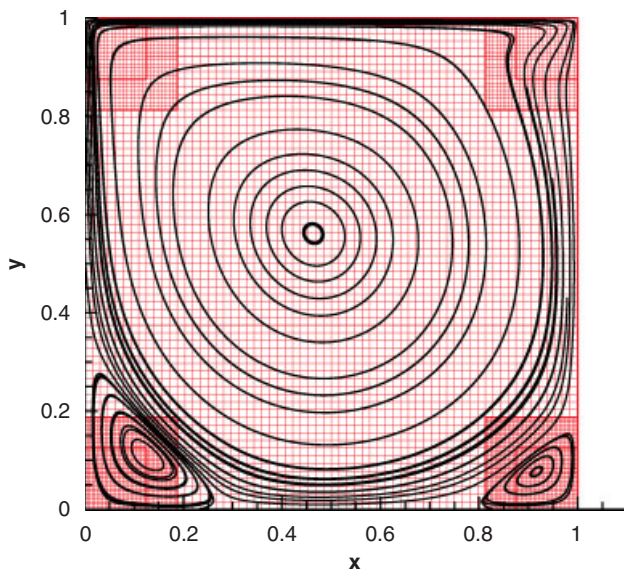

Figure 8. Streamlines on an block-structured mesh for the lid-driven cavity.

The main results found in the literature are given on the intensity and position of the vortices. The results are obtained with convergence criteria on stationarity below 10^{-12}. Our results are compared with the results obtained in [14] to exhibit the improvements of the method.

4.3.1. Position and intensity of the vortex. Tables I–III that represent the position of the vortices and the intensity of the streamlines show the good behaviour of the method in comparison with the results of the literature. We can observe in the two first lines of the table that both methods

DOI: 10.1002/fld

Table I. Intensity and position (x, y) of the main vortex.

Reference	Mesh size	Maximum streamline	x	y
Present	$121\,344 \simeq 348^2$	0.11885	0.4687	0.5664
Romé *et al.* [14]	$121\,344 \simeq 348^2$	0.11877	0.4687	0.5664
Botella and Peyret [20]	128^2	0.11894	0.4692	0.5652

Table II. Intensity and position (x, y) of the left secondary vortex.

Reference	Mesh size	Minimum streamline	x	y
Present	$121\,344 \simeq 348^2$	-1.7285×10^{-3}	0.1354	0.1119
Romé *et al.* [14]	$121\,344 \simeq 348^2$	-1.7285×10^{-3}	0.1354	0.1120
Botella and Peyret [20]	128^2	-1.7297×10^{-3}	0.1360	0.1118

Table III. Intensity and position (x, y) of the left ternary vortex.

Reference	Mesh size	Maximum streamline	x	y
Present	$121\,344 \simeq 348^2$	4.6742×10^{-8}	0.00757	0.00755
Romé *et al.* [14]	$121\,344 \simeq 348^2$	4.7314×10^{-8}	0.00781	0.00781
Botella and Peyret [20]	128^2	5.0399×10^{-8}	0.00768	0.00765

give very close results. The utility of the refinement is clear since it provides an amplitude of 10^{-8} for the right ternary vortex.

4.3.2. Velocity and pressure profiles. In Figure 9, the velocity profiles present a good accordance with those obtained by Botella and Peyret [20] and from a monoblock mesh with a Chebyshev polynomial step size variation. In [14], the authors observed that the pressure was discontinuous on the interface of the upper blocks because the incompressibility constraint did not equal zero. Figure 10 clearly shows the improvement of the method since the pressure is now continuous.

4.4. Laminar flow over a two-dimensional obstacle

The experimental configuration is presented in Figure 11. This flow was experimentally studied by Carvalho *et al.* [21]. The Reynolds number based on the height of the obstacle and mean axial velocity is 82.5. A recirculation appears behind the obstacle and when the Reynolds number increases, a second recirculation appears on the upper wall (see Figure 12). The boundary conditions at the inlet are prescribed as a parabolic profile for the axial velocity u and zero for the velocity v. At the outlet, a Neumann condition is imposed on both velocity components. In the present study, a mesh composed of three structured blocks is considered. Even if this configuration can be treated with an uniformly refined grid, we have chosen this test case to prove the robustness of our approach by putting the interface between blocks in a strong shear zone. Indeed, for complex flows and geometries, the fact that vortices cross the interface is very frequent. The grid is fine around the obstacle and stretched near the inlet and the outlet (see Figure 12). The total number of elements is 131 040.

DOI: 10.1002/fld

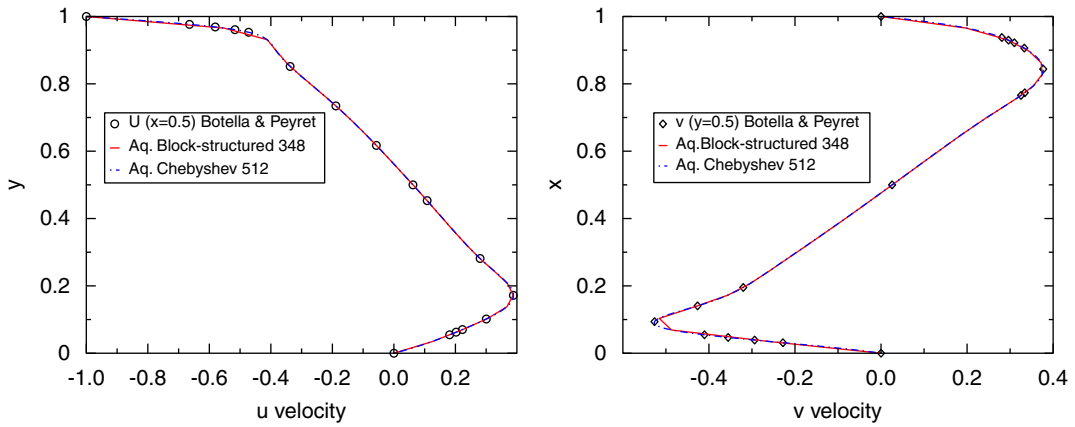

Figure 9. u profiles at $x=0.5$ (left) and v profiles at $y=0.5$ (right).

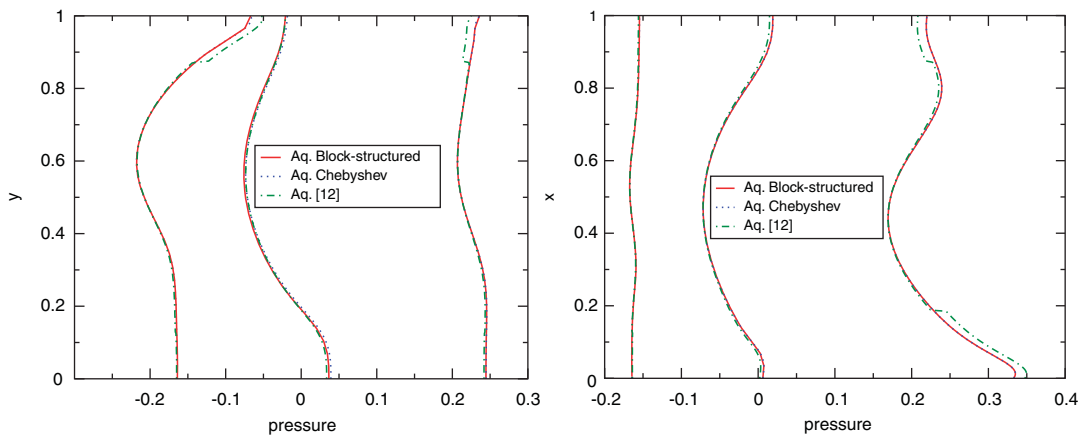

Figure 10. Pressure profiles at $x=0.1, 0.5, 0.9$ (left) and at $y=0.1, 0.5, 0.9$ (right).

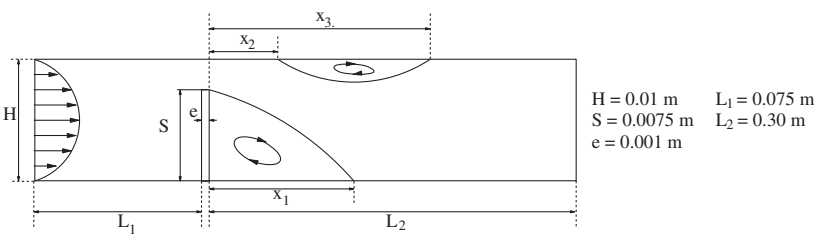

Figure 11. Global features of the flow over a two-dimensional obstacle.

Figure 13 presents the axial velocity u at different locations x/S measured [21] and computed. Table IV compares the reattachment lengths. Satisfactory results can be observed in comparison with the experimental data except for the reattachment length x_2/S. Several authors [22–24] have

DOI: 10.1002/fld

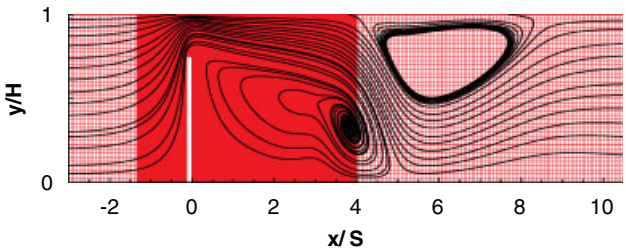

Figure 12. Streamlines on a block-structured mesh for the flow over a two-dimensional obstacle.

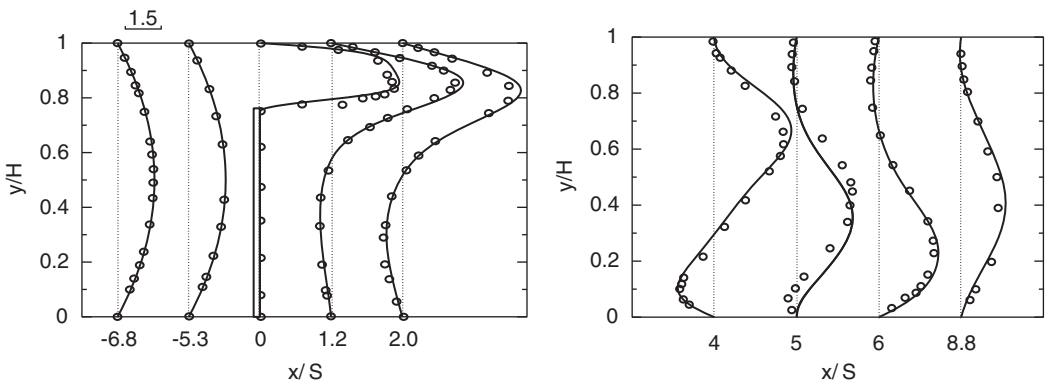

Figure 13. Comparison between calculation (—) and experimental data [21] (○) for flow over the fence ($Re = 82.5$).

Table IV. Comparison of the reattachment lengths.

	x_1/S	x_2/S	x_3/S
Present	4.96	4.12	8.38
Aq. monoblock 1800×200	4.99	4.01	9.19
Carvalho *et al.* [21]	5.00	2.01	10.4

considered this flow to validate their scheme but they have only compared the axial velocity u at different locations x/S and none of them has measured the recirculation lengths. Consequently, we cannot really verify if the difference on x_2/S comes from our computation or from the measurement in [21]. At least, multiblock results are coherent (see Table IV) with those obtained on a fine monoblock grid, solved with a different velocity–pressure coupling (augmented lagrangian).

4.5. Flow past a triangular cylinder

Flow past a equilateral triangular cylinder was studied. The Reynolds number is based on the side of the triangular cylinder ($h = 1$) and the axial velocity inlet ($u = 0.5$). We focussed on two flow

DOI: 10.1002/fld

ranges according to the value of the Reynolds number in relation to its critical value Re_c:

- $Re < Re_c$: the flow is stationary. Two steady symmetrical vortices can be observed behind the cylinder: their size increases with increasing Re.
- $Re \geqslant Re_c$: the flow becomes unsteady and periodic. Two vortices form at the rear-end vertices of the cylinder and are shed alternately.

Jackson [25] studied the onset of vortex shedding in flow past variously shaped bodies. For an isosceles triangle with base 1 and height 0.8, he reported a critical Reynolds as 34.318 and a corresponding Strouhal number as 0.13554. Zielinska and Wesfreid [26] computed flow past an equilateral triangle with a blockage ratio equal to $\frac{1}{15}$ and found a critical Reynolds number of 38.3. De and Dalal [27] carried out a similar study and calculated a critical Reynolds number of 39.9 for a blockage ratio of $\frac{1}{20}$. This case was chosen here because most studies have dealt with flow past circular or square cylinders and laminar flow past a triangular cylinder has not been intensively studied so far. Moreover, this configuration is well adapted to validate and illustrate the utility of block-structured meshes.

4.5.1. Parameters of the case test. Figure 14 represents the block-structured mesh used in this case. The grid is fine around the cylinder and space step size increases in front of and behind it. The number of grid nodes distributed over a side of the cylinder is 100. The total number of elements is 137 980. At the inlet, a flat profile is imposed for the axial velocity u and zero for the velocity v. At the outlet, a Neumann condition is imposed on both velocity components. We will compare the results with [27].

4.5.2. Steady flow. The streamlines in the vicinity of the cylinder for two Reynolds numbers are shown in Figure 15.

To assess the method, the recirculation length (L_r) defined by the reattachment of the fluid was measured and a linear relationship between L_r and Re obtained in [27] (see Figure 16). The results seem to be in good accordance with those presented in [27].

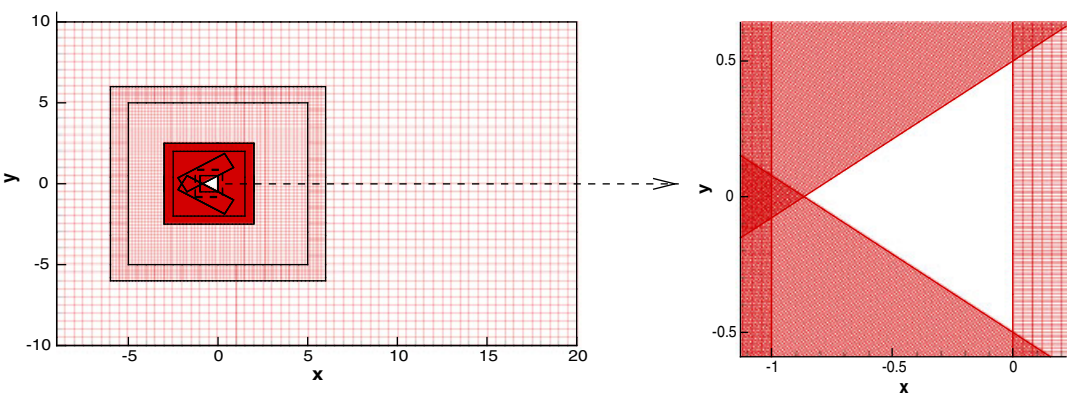

Figure 14. Block-structured mesh for flow past a triangular cylinder.

DOI: 10.1002/fld

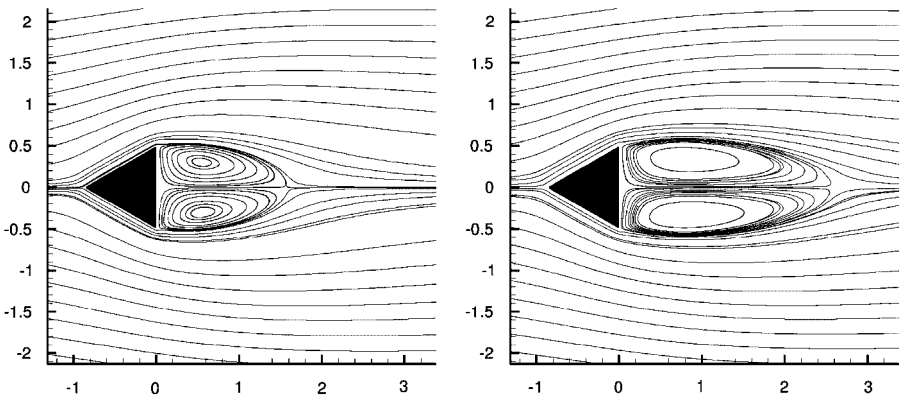

Figure 15. Steady-state streamlines $Re = 20$ (left), $Re = 35$ (right).

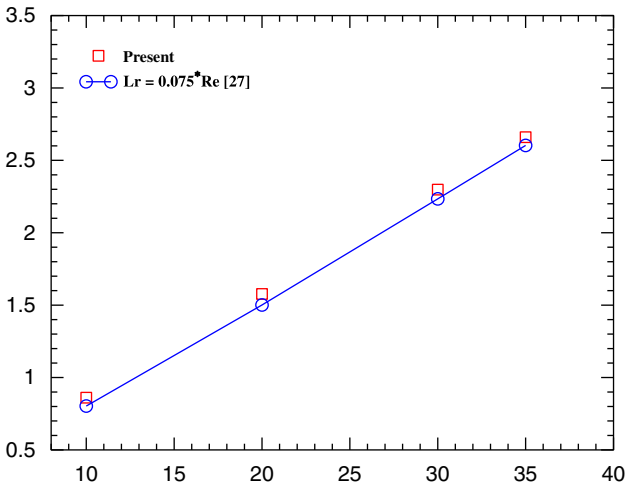

Figure 16. $L_r - Re$ relationship.

Table V. Comparison of the results for $Re = 100$.

	C_D	C_{D_p}	$C_{L_{rms}}$	St
Present	1.6698	1.3579	0.2626	0.1960
De and Dalal [27]	1.7549	1.2986	0.2974	0.1962

4.5.3. Unsteady and periodic flow. The flow becomes unsteady and periodic for $Re \geqslant 40$. For $Re = 100$, the time-average drag coefficient (C_D), time-average pressure drag coefficient (C_{D_p}), rms of the lift coefficient ($C_{L_{rms}}$) and the Strouhal number (St) are compared with [27]. We can see in Table V difference below 5% except for the $C_{L_{rms}}$ where the gap is 11%. It can be explained

DOI: 10.1002/fld

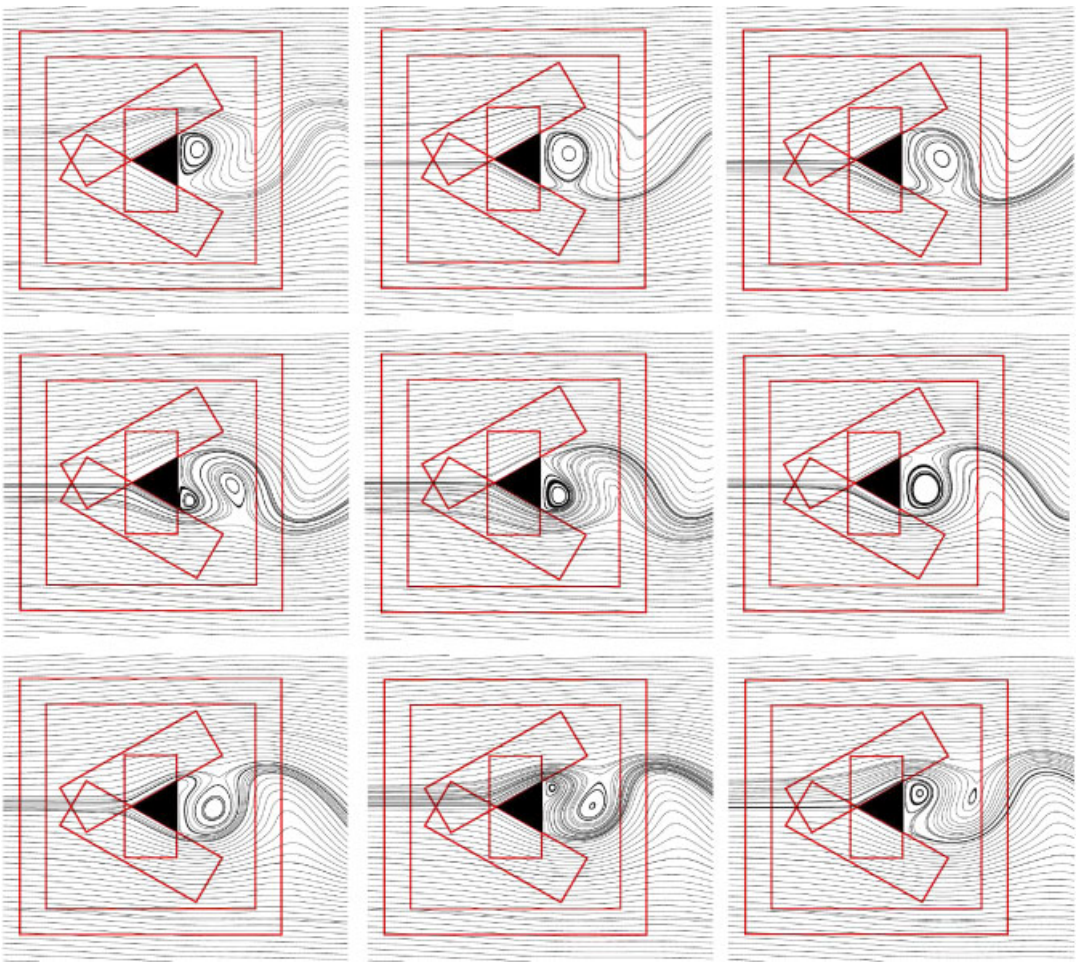

Figure 17. Streamlines for the flow past a triangular cylinder during a period at $Re = 100$ (it reads from left to right and vertically).

by the difference of the mesh size and the numerical method used by the authors. We can notice that ensuring the continuity of the pressure between blocks allowed us to compute the drag and lift coefficients even if the contours of the geometry are described by several blocks (contrary to the previous method where jumps of pressure between blocks were observed).

Finally, Figure 17 shows the streamlines around the triangular cylinder during a period at $Re = 100$ giving prominence to the periodicity of the flow.

5. CONCLUSION

In this paper, we have proposed an improvement of a method first introduced by Romé *et al.* in [14]. Both methods deal with a domain decomposition technique for non-conforming and

DOI: 10.1002/fld

overlapping block-structured meshes. They are non-iterative and based on a implicit non-conservative interpolation of the variables at the interfaces. The linear systems are modified in comparison with those obtained on a monoblock mesh since lines are added to take into account the connectivity between blocks.

The main difference between the two methods is the velocity–pressure coupling. In [14], the authors dealt with this coupling by an augmented Lagrangian method. In some cases, the divergence of the velocity at the interfaces between blocks was not null leading to a discontinuity for the pressure. In the present study, velocity and pressure were coupled by a pressure correction scheme. The divergence of velocity is now null over the whole domain and the discontinuity of pressure has disappeared. In many cases, the gradient of the pressure is sufficient to carry on computations but an accurate pressure is needed to compute physical parameters such as drag and lift coefficients for example. Consequently, the proposal method improves this point. Several numerical tests were carried out in order to validate the method. They clearly showed its feasibility and accuracy.

ACKNOWLEDGEMENTS

The authors thank Professor Mejdi Azaïez for his critical reading, helpful suggestions and fruitful discussions that guided us to achieve this work. We acknowledge calculation facilities financially supported by the Conseil Régional d'Aquitaine and the French Ministry of Research and Technology.

REFERENCES

1. Quarteroni A, Valli A. *Domain Decomposition Methods for Partial Differential Equations*. Oxford University Press: Oxford, 1999.
2. Schwarz HA. Über einen Grenzbergang durch alternirendes Verfahren. *Vierteljahrsschrift der Naturforschenden Gesellschaft in Zürich* 1870; **15**:272–286.
3. Lions PL. On the Schwarz alternating method III: a variant for nonoverlapping subdomains. *Third International Symposium on Domain Decomposition Methods for Partial Differential Equations*, Philadelphia, 1990.
4. Bernardi C, Maday Y, Patera AT. Domain decomposition by the mortar element method. In *Asymptotic and Numerical Methods for Partial Differential Equations with Critical Parameters*, Kaper HG, Garbey M (eds). NATO ASI Series C, vol. 384. Kluwer Academic Publishers: Dordrecht, 1993; 269–286.
5. Cai XC, Dryja M, Sarkis M. Overlapping nonmatching grid mortar element methods for elliptic problems. *SIAM Journal on Numerical Analysis* 1999; **36**:581–606.
6. Benek JA, Buning PG, Steger JL. A 3-D chimera grid embedding technique. *AIAA 85-1523CP*, 1985.
7. Steger JL, Benek JA. On the use of composite grid schemes in computational aerodynamics. *Computer Methods in Applied Mechanics and Engineering* 1987; **64**:301–320.
8. Lilek Z, Muzaferija S, Peric M, Seidl V. An implicit finite-volume method using nonmatching blocks of structured grid. *Numerical Heat Transfer* 1997; **32**:385–401.
9. Usera G, Vernet A, Ferré JA. A parallel block-structured finite volume method for flows in complex geometry with sliding interfaces. *Flow Turbulence Combustion* 2008; **81**:471–495.
10. Tang HS, Casy Jones S, Sotiropoulos F. An overset-grid method for 3D unsteady incompressible flows. *Journal of Computational Physics* 2003; **191**:567–600.
11. Tang HS. Study on a grid algorithm for solution of incompressible Navier–Stokes equations. *Computers and Fluids* 2006; **35**:1372–1383.
12. Henshaw WD, Watson TJ. A fourth-order accurate method for the incompressible Navier Stokes equations on overlapping grids. *Journal of Computational Physics* 1994; **113**:13–25.
13. Romé C, Glockner S. An implicit multiblock coupling for the incompressible Navier–Stokes equations. *International Journal for Numerical Methods in Fluids* 2005; **47**:1261–1267.
14. Romé C, Glockner S, Caltagirone JP. Resolution of the Navier–Stokes equations on block-structured meshes. *International Journal for Numerical Methods in Fluids* 2007; **54**:1239–1268.

DOI: 10.1002/fld

15. Fortin M, Glowinski R. *Méthodes de Lagrangien Augmenté*, *Applicationà la résolution numérique de problèmes aux limites*. Collection Méthodes Mathématiques de l'Informatique. Dunod: Paris, 1982.
16. Timmermans LJP, Minev PD, Van De Vosse FN. An approximate projection scheme for incompressible flow using spectral elements. *International Journal for Numerical Methods in Fluids* 1996; **22**:673–688.
17. Harlow FH, Welch JE. Numerical calculation of time-dependent viscous incompressible flow of fluid with free surface. *Physics of Fluids* 1965; **8**:2182–2189.
18. Amestoy PR, Duff IS, L'Excellent JY. Multifrontal parallel distributed symmetric and unsymmetric solvers. *Computer Methods in Applied Mechanics and Engineering* 2000; **184**:501–520.
19. Caltagirone JP, Breil J. Sur une méthode de projection vectorielle pour la résolution des équations de Navier–Stokes. *Comptes Rendus de l'Académie des Sciences*, *Série II*, *Paris* 1999; **327**:1179–1184.
20. Botella O, Peyret R. Benchmark spectral results on the lid-driven cavity flow. *Computers and Fluids* 1998; **4**:421–433.
21. Carvalho MG, Durst F, Pereira JC. Predictions and measurements of laminar flow over two-dimensional obstacles. *Applied Mathematical Modelling* 1987; **11**:23–34.
22. Song B, Liu GR, Lam KY, Amano RS. On a higher-order bounded discretization scheme. *International Journal for Numerical Methods in Fluids* 2000; **32**:881–897.
23. N'Dri D, Garon A, Fortin A. Incompressible Navier–Stokes computations with stable and stabilized space–time formulations: a comparative study. *Communications in Numerical Methods in Engineering* 2002; **18**:495–512.
24. Rida S, McKenty F, Meng FL, Reggio M. A staggered control volume scheme for unstructured triangular grids. *International Journal for Numerical Methods in Fluids* 1997; **25**:697–717.
25. Jackson CP. A finite-element study of the onset of vortex shedding in flow past variously shaped bodies. *Journal of Fluid Mechanics* 1987; **182**:23–45.
26. Zielinska BJ, Wesfreid JE. On the spatial structure of global modes in wake flow. *Physics of Fluids* 1995; **7**:1418–1424.
27. De AK, Dalal A. Numerical simulation of unconfined flow past a triangular cylinder. *International Journal for Numerical Methods in Fluids* 2006; **52**:801–821.

DOI: 10.1002/fld